Factors Affecting Validity of PVG-Power Settling Time Estimation in Designing MPP-tracking Perturbation Frequency

***Abstract*—An open-loop and closed-loop operating boost-power-stage converter with relatively low damping factor exhibit resonant behavior in transient conditions. Such a undamped transient characteristic introduces overshoot to control-to-output-variable transfer function which is also visible in the inductor current transient behavior. Therefore, due to the either too large duty ratio or voltage-reference step change, the inductor current can move from continuous conduction mode to discontinuous conduction mode. That transforms second-order system into an equivalent first-order dynamic system extending the PV-power settling time significantly and reducing power tracking performance of the system. This paper introduces design guidelines to determine maximum perturbation step size for duty ratio and input-voltage reference under open-loop and closed-loop operation, respectively. Two different closed-loop design examples are considered in this paper, based on the application of pure integral controller with phase margin (PM) close to 90 degrees and proportional-integral-derivative controller with PM close to 40 degrees, respectively. The closed-loop system dynamics is known to be characterized by the dominating poles and zeros, which locate closest to the origin. This means that the closed-loop system can be usually characterized by the well-known second-order transfer function. Therefore, the minimum and maximum overshoot of the inductor current can be well approximated as demonstrated by deterministic analysis and experimental results.**

I. Introduction

The solar energy systems are usually operated at the maximum power point (MPP) of their photovoltaic (PV) generator [1]–[3] or at the maximum power (MP) stipulated by the coordinating system controller for preventing the grid overvoltage to take place [4]–[7]. Due to the highly nonlinear nature of the PV generator and varying environmental conditions in terms of irradiance, ambient temperature, passing by clouds, etc., the validity of every operation point has to be checked by means of the proper method. The most frequently applied perturbative MP-tracking methods are the perturb and observe (P&O) and incremental conductance methods, where the PV voltage is perturbed and the corresponding changes in PV power is observed for mapping the location of the operation point within the current-voltage (I-V) curve of the PV generator as well as the direction, where to go for satisfying the set goal [1], [2]. In this respect, the parameters, which have to be designed, are the frequency of the perturbation (i.e., the time interval between the consecutive perturbation instants) and its step size [3]. As discussed in [8]–[12], the maximum perturbation frequency should be selected according to the settling time of the PVG power transient induced by the injected perturbation, as well as the minimum perturbation step size depends on the maximum expected irradiation variation rate and resolution of the converter analog-to-digital converters. Perturbation step size should be reduced as long as the change in the PVG power induced by the perturbation step is higher than that induced by irradiation change.

In addition to the minimum perturbation step size, the upper limit also exists. In the grid-connected solar energy systems, one common approach is to use double-stage conversion, in which there is the single-phase or three-phase inverter in cascaded with the boost-power stage converter. In this way, larger variations in input voltage can be tolerated and the maximum input voltage can be smaller compared to the single-stage conversion consisting only the inverter [13]. Other benefits of the boost topology in photovoltaic applications are that the input current is continuous and that blocking diode is included in the topology so that no additional diode is needed. The purpose of blocking diode is to prevent current from flowing back to the PVG during the night or other times of low irradiation [14]. However, the open-loop and closed-loop boost-power-stage converter operating with relatively low damping factor exhibit resonant behavior in transient conditions. Such a undamped transient characteristic introduces overshoot to control-to-output-variable transfer function which is also visible inherently in the inductor current transient behavior. Therefore, due to the either too large duty ratio or voltage-reference step change, the inductor current can move from continuous conduction mode (CCM) to discontinuous conduction mode (DCM). That transforms the second-order system into an equivalent first-order dynamic system extending the PV-power settling time significantly, thus, reducing power tracking performance and violating the validity of the theory developed for PVG-power settling time estimation for open-loop [15] and closed-loop [16] converters.

This paper introduces design guidelines to determine maximum step changes for duty ratio and input-voltage reference under open-loop and closed-loop operation. Two different design examples are considered in this paper, based on the application of pure integral (I) controller with phase margin (PM) close to 90 degrees and proportional-integral-derivative (PID) controller with PM close to 40 degrees, respectively. The closed-loop system dynamics is known to be characterized by the dominating poles and zeros, which locate closest to the origin. By means of previously developed techniques to extract system damping factor and natural frequency [15]–

[17], solving maximum perturbation step size becomes a trivial task.

II. General Dynamics of PV Power

Considering small perturbations in PV power, the small-signal PV power can be written as [3]

$$\hat{p}_{\rm pv} = V_{\rm pv}\hat{i}_{\rm pv} + I_{\rm pv}\hat{v}_{\rm pv} + \hat{v}_{\rm pv}\hat{i}_{\rm pv}, \tag{1}$$

which can be derived from the definition of power in terms of voltage and current (i.e. $p_{\rm pv} = (V_{\rm pv} + \hat{v}_{\rm pv})(I_{\rm pv} + \hat{i}_{\rm pv})$) and discarding the steady-state value at the operation point. If considering only the dynamic behavior of the PV power induced by a step-change at the operation point of the DC-DC converter (i.e. irradiance and output voltage variations of DC-DC converter are neglected) then (1) can be given by

$$\hat{p}_{\rm pv} \approx V_{\rm pv}\left(\frac{1}{R_{\rm pv}} - \frac{1}{r_{\rm pv}}\right)\hat{v}_{\rm pv} - \frac{\hat{v}_{\rm pv}^2}{r_{\rm pv}}, \tag{2}$$

because $\hat{i}_{\rm pv} \approx -(1/r_{\rm pv})\hat{v}_{\rm pv}$ and static PV resistance equals $R_{\rm pv} = U_{\rm pv}/I_{\rm pv}$. According to (2), we can state that the PV power ripple can be defined in CCR by $\hat{p}_{\rm pv} \approx I_{\rm pv}\hat{v}_{\rm pv}$, in CPR by $\hat{p}_{\rm pv} \approx -\hat{v}_{\rm pv}^2/R_{\rm pv}$, and in CVR by $\hat{p}_{\rm pv} \approx (-V_{\rm pv}/r_{\rm pv})\,\hat{v}_{\rm pv} = V_{\rm pv}\hat{i}_{\rm pv}$ based on the behavior of $r_{\rm pv}$ and $R_{\rm pv}$ at the different operation points of the PV generator. [15]

Fig. 1 shows the effect of the PV-voltage perturbation on the PV power around the MPP. According to the figure, the ripple of PV power is constant and in phase with the PV-voltage ripple in CCR, zero at MPP and increasing along the increase in PV voltage with 180° phase shift with the PV-voltage ripple in CVR, respectively. This kind of behavior is exactly as the developed PV-power-ripple in (2) predicts to be happening. The same phenomenon is also utilized in MPPT technique called ripple correlation control [18]. By observing the vicinity of the MPP in Fig. 1, it can be noticed that MPP is not just a point but a narrow region (i.e., CPR).

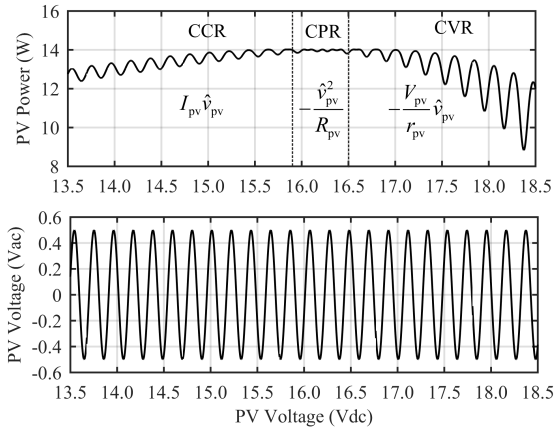

Fig. 1. Extended view of PV-voltage-induced PV-power ripple at the operating points in the vicinity of the CPR.

III. PV-Interfacing Converter Operating at Open Loop

The boost-power-stage converter shown in Fig. 2a is commonly used as an MPP-tracking converter. The open-loop operating boost-power-stage converter exhibits resonant behavior in the transient conditions, which extends the settling process of PV voltage and current. The transient behavior can be studied from the linear dynamical representation of the PV-generator-converter interface depicted in Fig. 2b, which is discussed more detail in [19], [20].

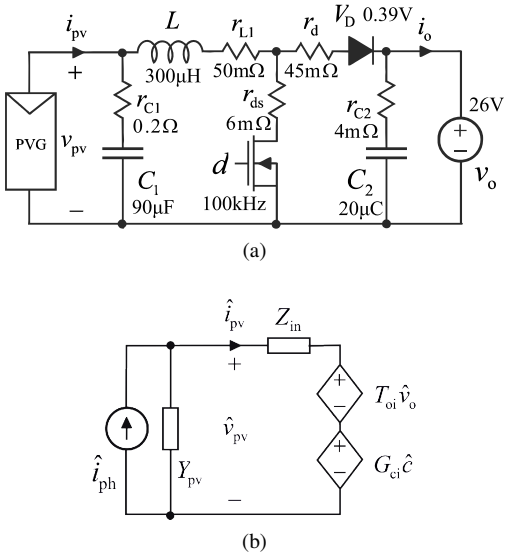

Fig. 2. Illustration of (a) PV-generator-interfacing boost-power-stage converter and (b) a dynamic representation of the PV-generator-converter interface.

According to the figure, we can compute that the dynamics related to the PV voltage and current can be given as follows

$$\begin{aligned}\hat{v}_{\rm pv} &= \frac{Z_{\rm in}}{1+Z_{\rm in}Y_{\rm pv}}\hat{i}_{\rm ph} + \frac{T_{\rm oi}}{1+Z_{\rm in}Y_{\rm pv}}\hat{v}_{\rm o} + \frac{G_{\rm ci}}{1+Z_{\rm in}Y_{\rm pv}}\hat{c}\\ \hat{i}_{\rm pv} &= \frac{1}{1+Z_{\rm in}Y_{\rm pv}}\hat{i}_{\rm ph} - \frac{Y_{\rm pv}T_{\rm oi}}{1+Z_{\rm in}Y_{\rm pv}}\hat{v}_{\rm o} - \frac{Y_{\rm pv}G_{\rm ci}}{1+Z_{\rm in}Y_{\rm pv}}\hat{c},\end{aligned} \tag{3}$$

where $Z_{\rm in}$ is the input impedance of the converter, $T_{\rm oi}$ is the output-to-input transfer function and $G_{\rm ci}$ refers to control-to-PV-voltage transfer function. As the converter operates at open loop, the control variable is duty ratio (i.e. $\hat{c} = \hat{d}$). It is well known that the temperature of the PV modules has significant effect on the PV power but its dynamics is quite slow due to the large thermal capacity of the PV panels as discussed also in [3]. Therefore, its effect is not considered in (3). From the perturbation-frequency design point of view, the control-to-input-voltage-related dynamics is of interest in (3) (i.e., the last terms of the equations in (3)).

The experimental transient waveforms of PV voltage, current, and power shown in Fig. 3 clearly confirms the validity of the theoretical formulation for the behavior of the PV-power transient in the different operational regions discussed in more detail in [15]. Fig. 3 is constructed in such a manner that all the original waveforms are divided by their final values to

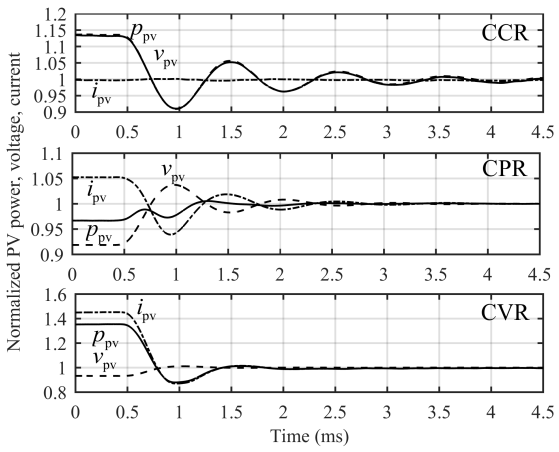

Fig. 3. Behavior of PV voltage (dashed line), current (dash-dotted line), and power (solid line) when a step change in a duty ratio is applied in a duty-ratio-operated boost-power-stage converter in different PV-generator operational regions. [15]

maximize the information of the settling behavior: In CCR, the PV-power transient follows directly the settling behavior of the PV voltage. In CPR, the PV-power transient is very small, because the PV-voltage and current behaviors tends to cancel each other. In CVR, the PV-power transient follows directly the settling behavior of the PV current. The PV-power settling time is also longest in CCR, which is clearly visible in Fig. 3 . The changes in the settling time are induced by the changes in the damping behavior of the internal resonance due to the PV-generator dynamic resistance, which affects the time constant of the system i.e., $\tau = 1/\zeta_{\rm pv}\omega_{\rm n}$ (i.e., $\zeta_{\rm pv}$ denotes the PVG-affected damping factor and $\omega_{\rm n}$ denotes the undamped natural frequency). The PV-generator-affected damping factor of a duty-ratio or voltage-mode-controlled (DDR/VMC) converter can be given in general by [20]

$$\zeta_{\rm pv} \approx \frac{1}{2}\left(r_{\rm loss}\sqrt{\frac{C_1}{L}} + \frac{1}{r_{\rm pv}}\sqrt{\frac{L}{C_1}}\right), \tag{4}$$

where $r_{\rm loss} = r_{\rm L}+r_{\rm C1}+Dr_{\rm ds}+(1-D)r_{\rm D}$ denotes the parasitic losses of the power-stage components as well as L and C_1 denote the power stage inductance and capacitance values, respectively. As shown in [20]–[22], while PVG dynamic resistance greatly affects the damping factor, its influence on the DC gain and natural frequency is insignificant.

According to [20], when PVG is connected to an interfacing power converter, the control-to-input voltage transfer function of the combined system is given by (cf. (3))

$$G^{\rm pv}_{\rm ci-o}(s) = \frac{G_{\rm ci-o}}{1+Z_{\rm in}Y_{\rm pv}} = -V_{\rm e}\frac{\omega_{\rm n}^2(1+s/\omega_{\rm z-esr})}{s^2+2\zeta_{\rm pv}\omega_{\rm n}s+\omega_{\rm n}^2}, \tag{5}$$

where $\omega_{\rm n} = 1/\sqrt{LC_1}$ is undamped natural frequency of the converter and $\omega_{\rm z-esr}$ is the ESR zero induced by input capacitor. Since, PVG voltage transient response in Laplace domain is $\hat{v}_{\rm pv}(s) = G^{\rm pv}_{\rm ci-o}\cdot\hat{d}$ and the longest settling time of PVG power occurs in CCR where $\hat{p}_{\rm pv} \approx I_{\rm pv}\hat{v}_{\rm pv}$, we can approximate the time where the PV power is settled to $(1-\Delta)\cdot 100$ % from its final value as follows [15], [17]

$$\begin{aligned} T_\Delta &= \frac{1}{\zeta_{\rm pv}\omega_{\rm n}}\ln\frac{\sqrt{1+\frac{\omega_{\rm n}}{\omega_{\rm z-esr}}\left[\frac{\omega_{\rm n}}{\omega_{\rm z-esr}}-2\zeta_{\rm pv}\right]}}{\Delta\sqrt{1-\zeta_{\rm pv}^2}} \\ &\approx \frac{1}{\zeta_{\rm pv}\omega_{\rm n}}\ln\frac{1}{\Delta\sqrt{1-\zeta_{\rm pv}^2}}, \end{aligned} \tag{6}$$

In order to accurately predict the PV settling time process, Eq. (6) assumes continuous conduction mode, i.e., inductor current does not reach zero during the transient. However, it will shown in the following analysis that discontinuous inductor can extend the PV power settling process significantly.

A. Determining Maximum Duty Ratio Step Change

If assuming that the PV generator is an ideal current source (i.e., in CCR) then the open-loop control-to-inductor-current transfer function $G_{\rm cL-o}$ can be solved similarly as in [20] by

$$G_{\rm cL-o} = \frac{V_{\rm e}\omega_{\rm n}^2C_1 s}{s^2+2\zeta_{\rm pv}\omega_{\rm n}s+\omega_{\rm n}^2} = \frac{C_1 s}{1+s/\omega_{\rm z-esr}}\cdot G_{\rm ci-o}. \tag{7}$$

Hence, the PV-voltage transient induced by a step change in the duty ratio can be given in Laplace domain as follows

$$i_{\rm L}(s) = \frac{V_{\rm e}\omega_{\rm n}^2C_1 s}{s^2+2\zeta\omega_{\rm n}s+\omega_{\rm n}^2}\cdot\frac{\Delta d}{s} \tag{8}$$

According to (8), we can estimate the time-domain behavior of $i_{\rm L}$ when a step change in duty ratio is applied. By utilizing inverse Laplace operator to (8), we get

$$\begin{aligned} &i_{\rm L}(t) = \\ &-V_{\rm e}C_1\left(\frac{\omega_{\rm n}}{\sqrt{1-\zeta_{\rm pv}^2}}\exp\left(-\zeta_{\rm pv}\omega_{\rm n}t\right)\sin\left(\omega_{\rm n}\sqrt{1-\zeta_{\rm pv}^2}\right)\right)\Delta d, \end{aligned} \tag{9}$$

Figure 4 represents simulated PV voltage, inductor current and capacitor current transient waveforms when two different duty ratio step changes are applied in the boost-power-stage converter in Fig. 2a. Black lines indicate the condition where inductor current just reaches the zero due duty-ratio step change Δd. In contrast, red lines represent the case where Δd is too large causing the inductor current to move discontinuous continuous mode. Due to the diode included inherently in the power-stage (cf., Fig. 2a), the inductor current cannot drop below zero. Since, capacitor current $i_{\rm C1} = I_{\rm pv} - i_{\rm L}$ remains constant, the inductor-current saturation transforms the second-order system into equivalent first-order dynamic system extending the PV-power settling time and reducing power tracking performance of the system.

The critical duty-ratio step change can be solved by analyzing the time-domain equation in (9). The time, where $i_{\rm L}$

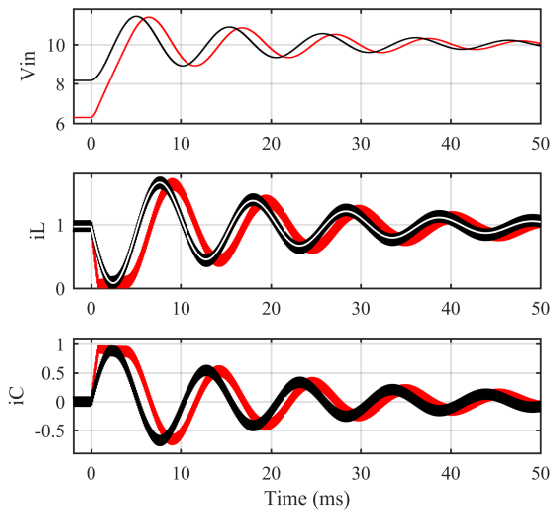

Fig. 4. Illustration of the transient response of the inductor current when critical (black line) and too large (red line) duty-ratio step change is applied. White line corresponds the estimated transient response based on (9).

in (9) reaches its minimum value, can be found by solving $di_{\mathrm{L}}(t)/dt = 0$. The minimum value for the unit-impulse response of the underdamped system occurs at [23]

$$t_{\min} = \frac{\tan^{-1}\left(\sqrt{1-\zeta_{\mathrm{pv}}^2}/\zeta_{\mathrm{pv}}\right)}{\omega_{\mathrm{n}}\sqrt{1-\zeta_{\mathrm{pv}}^2}}. \tag{10}$$

Thus, the minimum value for $i_{\mathrm{L}}(t)$ due to the duty-ratio step change is

$$i_{\mathrm{L}}(t_{\min}) = \underbrace{-V_{\mathrm{e}}C_1\omega_{\mathrm{n}}\exp\left(-\frac{\zeta_{\mathrm{pv}}}{\sqrt{1-\zeta_{\mathrm{pv}}^2}}\tan^{-1}\left(\frac{\sqrt{1-\zeta_{\mathrm{pv}}^2}}{\zeta_{\mathrm{pv}}}\right)\right)}_{M_{\mathrm{d}}}\cdot\Delta d. \tag{11}$$

To ensure continuous inductor current, the minimum inductor current after step change must be $\Delta i_{\mathrm{L}} = I_{\mathrm{pv}} - M_{\mathrm{d}}\cdot\Delta d - \Delta i_{\mathrm{L,pp}}/2 > 0$. The inductor current ripple $\Delta i_{\mathrm{L,pp}}$ is at its highest value when the input voltage is half the output voltage, i.e., $\Delta i_{\mathrm{L,pp}} = V_{\mathrm{o}}/(4Lf_{\mathrm{s}})$. Therefore, we can get the following equation for the maximum duty-ratio step size

$$\Delta d < \frac{I_{\mathrm{pv}} - V_{\mathrm{o}}/(8Lf_{\mathrm{s}})}{V_{\mathrm{e}}C_1\omega_{\mathrm{n}}\exp\left(-\frac{\zeta_{\mathrm{pv}}}{\sqrt{1-\zeta_{\mathrm{pv}}^2}}\tan^{-1}\left(\frac{\sqrt{1-\zeta_{\mathrm{pv}}^2}}{\zeta_{\mathrm{pv}}}\right)\right)}. \tag{12}$$

It can be noticed from (12) that the maximum duty-ratio step size depends both on converter parameters and voltage and current levels on its input and output. The worst case from the duty-ratio step change point of view occurs at low PV current (i.e. in low irradiance condition), where I_{pv} is the lowest.

IV. PV-Interfacing Converter Operating at Closed Loop

In a case of input-voltage-feedback-controlled converters, the PV-generator effect on the system damping behavior is quite different, especially, when the input-voltage-feedback-loop crossover frequencies are designed to be sufficiently lower or higher than the resonant frequency. The PV-generator effect to the closed-loop transfer functions can be attributed directly to $1/(1 + Z_{\mathrm{in-c}}Y_{\mathrm{pv}})$. The corresponding predicted frequency responses are given in Fig. 5, where the solid, dashed, and dash-dotted lines correspond to the operation in CCR, CPR, and CVR, respectively. Fig. 5 indicates clearly that the PV-generator effect on the converter dynamics in an input-voltage-feedback-controlled converter will be very small as discussed in [16]. Therefore, the set of equations in (3) becomes

$$\begin{aligned}\hat{v}_{\mathrm{pv}} &\approx Z_{\mathrm{in-c}}\hat{i}_{\mathrm{ph}} + T_{\mathrm{oi-c}}\hat{v}_{\mathrm{o}} + G_{\mathrm{ci-c}}\hat{c}\\ \hat{i}_{\mathrm{pv}} &\approx \hat{i}_{\mathrm{ph}} - Y_{\mathrm{pv}}T_{\mathrm{oi-c}}\hat{v}_{\mathrm{o}} - Y_{\mathrm{pv}}G_{\mathrm{ci-c}}\hat{c},\end{aligned} \tag{13}$$

where subscript extension 'c' denotes the closed-loop transfer functions.

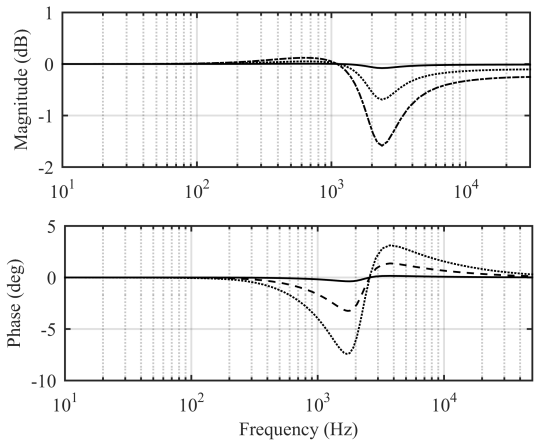

Fig. 5. Predicted PV-generator effect on the closed-loop transfer functions of an input-voltage-feedback-controlled boost power-stage converter (i.e., $1/(1+Z_{\mathrm{in-c}}/r_{\mathrm{pv}})$, where the crossover frequency of the input-voltage feedback loop is placed higher than the resonant frequency (i.e., 1 kHz vs. 3 kHz). [16]

Two different design examples are considered in this paper, based on the application of pure integral (I) controller with PM close to 90° and proportional-integral-derivative (PID) controller with PM close to 40°, respectively. In the case of I controller, the input-voltage feedback-loop crossover frequency would be less than the resonant frequency of the converter for providing sufficient attenuation at the resonant frequency (i.e., the resonant peak value should be less than -10 dB for eliminating the effect of the resonant on the settling behavior). This means that the damping factor would be rather high, because the PM would be close to 90°, and therefore, the roots of the second-order denominator would be well separated (i.e., $(s + \frac{\omega_{\mathrm{n}}}{2\zeta})(s + 2\zeta\omega_{\mathrm{n}}) = 0$).

In case the desired loop gain crossover frequency $\omega_{\rm c}$ is much lower than $\omega_{\rm p}$, integral (I) controller of the form

$$G_{\rm cc}^{\rm I} = \frac{K_{\rm cc}}{s} \tag{14}$$

Furthermore, in case $\omega_{\rm c} \ll \omega_{\rm p}$, there is no need to cancel the capacitor ESR induced zero and pure integrator may be utilized. In contrast, in case of PID control, the feedback-loop crossover frequency would be placed at the frequencies higher than the resonant frequency and the PM would be designed as desired.

$$G_{\rm cc}^{\rm PID} = \frac{K_{\rm cc}(1+s/\omega_{\rm z1})(1+s/\omega_{\rm z2})}{s(1+s/\omega_{\rm p1})(1+s/\omega_{\rm p2})} \tag{15}$$

Since the plant is underdamped, loop gain resonance peak must reside GM [dB] (gain margin) below zero to assure stability.

A. Approximated Dynamic Behavior of Closed-Loop System

In control engineering [23], the loop gain (L) and sensitivity function ($L/(1+L)$) are known as open and closed-loop feedback-loop gains, respectively. The closed-loop system dynamics is known to be characterized by the dominating poles and zeros, which locate closest to the origin. This means that the closed-loop system can be usually characterized by the well-known second-order transfer function as [16]

$$\frac{\omega_{\rm a}^2}{s^2 + s2\zeta\omega_{\rm a} + \omega_{\rm a}^2} \approx \frac{L}{1+L}, \tag{16}$$

where $\omega_{\rm a}$ and $\zeta_{\rm a}$ denote the undamped natural frequency and damping factor of the closed-loop system, respectively. It is worth noting that different subscript is used for the closed-loop system to differentiate those from open-loop counterparts. The corresponding open-loop loop gain with unity feedback and integral control action can be given by

$$L \approx \frac{\omega_{\rm a}^2}{s(s+2\zeta_{\rm a}\omega_{\rm a})}, \tag{17}$$

from which the crossover frequency ($\omega_{\rm c}$) and phase margin (PM) can be solved by setting the magnitude to unity (i.e., $|L|=1$), and solving the corresponding frequency and phase. The corresponding PM = $180^{\rm o} + \angle L(\omega_{\rm c})$ [23]. According to these procedures, $\omega_{\rm c}$ and PM can be given by

$$\begin{aligned} \omega_{\rm c} &= \omega_{\rm a}\sqrt{\sqrt{1+4\zeta_{\rm a}^4} - 2\zeta_{\rm a}^2} \\ {\rm PM} &= \tan^{-1}\left(\frac{2\zeta_{\rm a}}{\sqrt{\sqrt{1+4\zeta_{\rm a}^4} - 2\zeta_{\rm a}^2}}\right). \end{aligned} \tag{18}$$

According to (17), we need to know $\omega_{\rm a}$ and $\zeta_{\rm a}$ for solving the corresponding time-domain behavior (cf., (8)), which can be solved from (18) yielding [16]

$$\omega_{\rm a} = \frac{\omega_{\rm c}}{\sqrt{\sqrt{1+4\zeta_{\rm a}^4} - 2\zeta_{\rm a}^2}},\ \zeta_{\rm a} = \frac{\tan({\rm PM})}{2\big(1+\tan^2({\rm PM})\big)^{\frac{1}{4}}} \tag{19}$$

If assuming that the PV-power transient has to be attenuated within $(1\pm\Delta)$-times the final value before the next perturbation would take place then the corresponding settling times (T_Δ) can be computed to be [16]

$$\begin{aligned} T_\Delta^{\rm I} &= \frac{2\zeta_{\rm a}}{\omega_{\rm a}}\ln\left(\frac{1}{\Delta}\right) \\ T_\Delta^{\rm PID} &= \frac{1}{\zeta_{\rm a}\omega_{\rm a}}\ln\left(\frac{1}{\Delta\sqrt{1-\zeta_{\rm a}^2}}\right). \end{aligned} \tag{20}$$

B. Determining Maximum Input-Voltage Reference Step Change

In order to formulate equation for maximum input-voltage reference step change, corresponding closed-loop transfer function for inductor current need to be solved (cf., (8)). The closed-loop reference-to-inductor-current transfer function can be calculated based on open-loop transfer functions [20]

$$G_{\rm cL-c} = \frac{\hat{i}_{\rm L}}{\hat{v}_{\rm pv,ref}} = \frac{1}{G_{\rm se}}\frac{L}{1+L}\cdot\frac{G_{\rm cL-o}}{G_{\rm ci-o}} \tag{21}$$

The closed-loop transfer function $L/(1+L)$ can be approximated by (16) yielding

$$\begin{aligned} G_{\rm cL-c}^{\rm PID} &\approx -\frac{1}{G_{\rm se}}\cdot\frac{\omega_{\rm a}^2}{s^2+2\zeta_{\rm a}\omega_{\rm a}s+\omega_{\rm a}^2}\cdot\frac{C_1 s}{1+r_{\rm C1}C_1 s} \\ &\approx \frac{C_1\omega_{\rm a}^2 s}{s^2+2\zeta_{\rm a}\omega_{\rm a}s+\omega_{\rm a}^2}, 0<\omega<\omega_{\rm c} \end{aligned} \tag{22}$$

The final form in (22) can be achieved by the fact that pole of the capacitor is located much further from the origin and therefore, it will not affect the transient behavior. In case of I control, the roots of the second-order denominator are well separated and (22) can be represented as

$$G_{\rm cL-c}^{\rm I} \approx \frac{(C_1\omega_{\rm a}/2\zeta_{\rm a})s}{s+(\omega_{\rm a}/2\zeta_{\rm a})}, 0<\omega<\omega_{\rm c}. \tag{23}$$

Therefore, the time-domain transient response of $i_{\rm L}$ corresponds to exponential function where the only pole is located at $(\omega_{\rm a}/2\zeta_{\rm a})$. The inductor current time domain behavior can be solved from (22) similarly as in open loop yielding

$$\begin{aligned} &i_{\rm L}(t) = \\ &-C_1\left(\frac{\omega_{\rm a}}{\sqrt{1-\zeta_{\rm a}^2}}\exp\left(-\zeta\omega_{\rm a}t\right)\sin\left(\omega_{\rm a}\sqrt{1-\zeta^2}\right)\right)\cdot\Delta v_{\rm ref} \end{aligned} \tag{24}$$

Inductor current should not reach the zero during the transient due to voltage reference step size, i.e. $\Delta i_{\rm L} = I_{\rm pv} - M_{\rm v}\cdot\Delta v_{\rm ref} - \Delta i_{\rm L,pp}/2 > 0$. Therefore, the maximum voltage reference step change, which ensures CCM operation of the converter can be given as

$$\Delta v_{\rm ref} < \frac{I_{\rm L} - V_{\rm o}/(8Lf_{\rm s})}{C_1\omega_{\rm a}\exp\left(-\frac{\zeta_{\rm a}}{\sqrt{1-\zeta_{\rm a}{}^2}}\tan^{-1}\left(\frac{\sqrt{1-\zeta_{\rm a}^2}}{\zeta_{\rm a}}\right)\right)}. \tag{25}$$

V. Experimental Verification

The experimental measurements have been carried out by using a low-power MPPT boost converter supplied by a single PV module as illustrated in Fig. 6. Raloss SR30-36 PV module was used as a PVG, which is composed of 36 series-connected monocrystalline silicon cells. The PV module was illuminated by fluorescent lamps, which can produce maximum irradiance of about 500 $\mathrm{W/m^2}$ yielding short-circuit current of 1.0 A and open-circuit voltage of 19.2 V at module temperature of 45 °C. Further information about the panel can be found in [24]. The PV module is connected to the boost-power-stage prototype shown in Fig. 2a controlled by a digital signal processor (DSP). Voltage and current measurements were low-pass-filtered with the cut-off frequency of 50 kHz in order to prevent noise from converter switching action. Finally, the output of the converter is connected to the 26-V battery in parallel with Chroma 63103A current sink to maintain constant battery voltage.

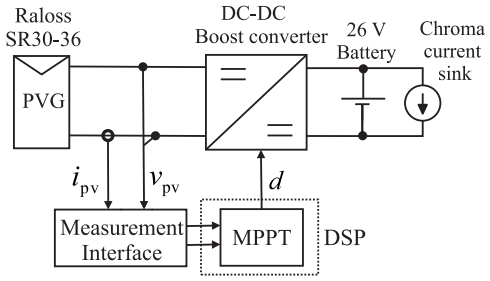

Fig. 6. Schematic representation of the experimental boost converter.

Figure 7 shows the PV voltage and inductor-current transient responses under three different duty ratio step changes. Based on the parameters listed in Fig. 2a, undamped natural frequency and damping factor can be calculated to be $6.086 \cdot 10^3\,\mathrm{rad/s}$ and 0.074, respectively. Thus, according to (12), the maximum duty-ratio step change can be calculated to be 0.075, which corresponds to 1V PV-voltage step change. Two other measured step responses are carried out by using half and double the critical step changes to highlight the effect of choosing too high duty-ratio step size. As can be seen from Fig. 7 and predicted in the prior analysis, the transient response of the PV voltage has similar settling time as long as the duty-ratio step change is lower than the critical step change. Moreover, Eq. (12) gives a good approximation for inductor current peak value. In contrast, it can be seen that inductor current is discontinuous, thus, increasing the settling time process of PV voltage and PV power. In contrast, it can be seen that the settling time process of PV voltage and PV power is extended due to the discontinuous inductor current.

The measured loop-gain transfer functions with PID controller can be seen in [16] providing more detailed information of the system. Based on the parameters listed in Fig. 2a and system characteristics listed in [16], the average crossover frequency and phase margin are $2\pi \cdot 2950$ rad/s and 35°, respectively. Therefore, PID-controlled closed-loop undamped

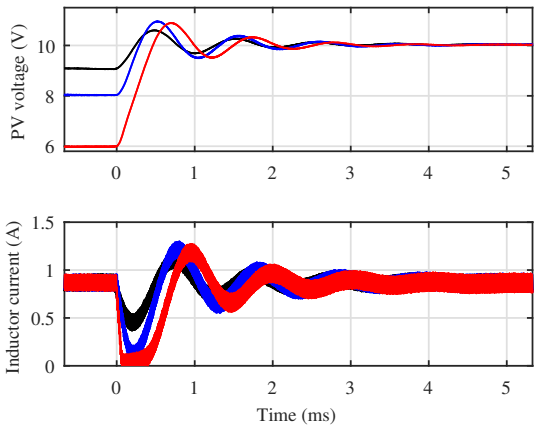

Fig. 7. Open-loop step responses of the PV voltage and inductor current when duty-ratio step changes of 0.037 (black line), 0.075 (blue line) and 0.150 (red line) are applied.

natural frequency and damping factor can be calculated to be $\omega_a = 2\pi \cdot 3263$ rad/s and $\zeta_a = 0.32$, obtained using (19). Thus, according to (25), the maximum voltage reference step change can be calculated to be 0.71V. Fig. 8 represents the closed-loop step responses when 0.5V, 0.71V and 3V PV-voltage-reference step changes are applied. The figure clearly indicates that too large perturbation step size causes delay in PV voltage transient response, thus, extending the settling time process.

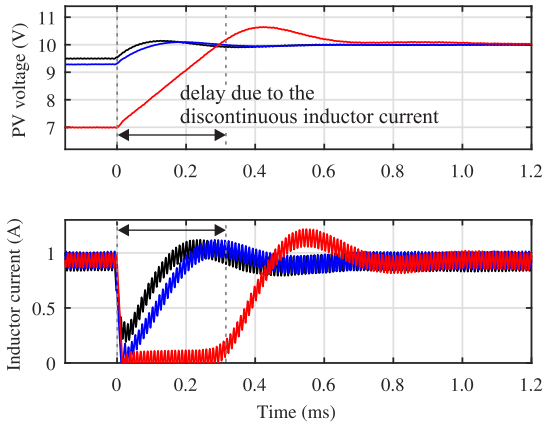

Fig. 8. The PV voltage and inductor-current step responses under PID control when 0.5V (black line), 0.71V (blue line) and 3V (red line) reference-voltage step changes are applied).

Finally, Fig. 9 shows PV voltage and inductor current step responses with I control. Gain of the integral controller is set to 6.3 yielding crossover frequency and PM to be $2\pi \cdot 28.6$ rad/s and 89.8°, respectively. With these values sufficient gain margin of 15dB is achieved. Based on (19), natural frequency and damping factor can be calculated to be $\omega_a = 2\pi \cdot 484$ rad/s and $\zeta_a = 8.46$. As can be predicted from the prior analysis, the transient response in Fig. 8 is overdamped and therefore, inductor current does neither induce any overshoot nor satu-

ration. Therefore, the predicted settling time ($T_{\Delta}^{\mathrm{I}} = 16.6$ ms) based on (20) matches well with experiments.

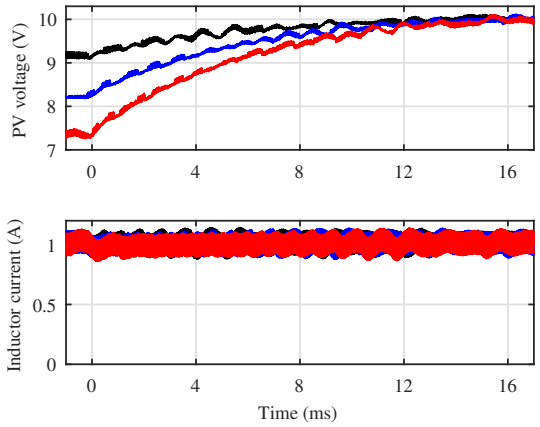

Fig. 9. The PV voltage and inductor-current step responses under I control when 0.9V (black line), 1.8V (blue line) and 2.7V (red line) reference-voltage step changes are applied.

VI. Conclusion

Due to the either too large duty-ratio or voltage-reference step change, the inductor current can move from CCM to DCM. That transforms second-order settling behavior into equivalent first-order settling behavior extending the PV-power settling time and thus, reducing the power-tracking performance and violating the validity of theory developed for PVG-power settling-time estimation for open-loop and closed-loop operated converters.

This paper introduces design guidelines to determine the maximum step sizes for duty ratio and input-voltage reference under open-loop and closed-loop operation. Two different design examples are considered in this paper, based on the application of pure integral controller with PM close to 90 degrees and proportional-integral-derivative controller with PM close to 40 degrees, respectively. The closed-loop system dynamics is known to be characterized by the dominating poles and zeros, which locate closest to the origin. This means that the closed-loop system can be usually characterized by utilizing well-known control engineering methods.

References

[1] S. Lyden and M. Haque, "Maximum power point tracking techniques for photovoltaic systems: a comprehensive review and comparative analysis," *Renew. Sustain. Energy Rev.*, vol. 52, pp. 1504–1518, 2015.

[2] P.-C. Chen, P.-Y. Chen, Y.-H. Liu, J.-H. Chen, and Y.-F. Luo, "A comparative study on maximum power point tracking techniques for photovoltaic generation systems operating under fast changing environments," *Sol. Energy*, vol. 119, pp. 261–276, Sep. 2015.

[3] N. Femia, G. Petrone, G. Spagnuolo, and M. Vitelli, "Optimization of perturb and observe maximum power point tracking method," *IEEE Trans. Power Electron.*, vol. 20, no. 4, pp. 963–973, Jul. 2005.

[4] A. Ahmed, L. Ran, S. Moon, and J.-H. Park, "A fast pv power tracking control algorithm with reduced power mode," *IEEE Trans. Energy Convers.*, vol. 28, no. 3, pp. 565–575, Sep. 2013.

[5] A. Sangwongwanich, Y. Yang, and F. Blaabjerg, "High-performance constant power generation in grid-connected pv systems," *IEEE Trans. Power Electron.*, vol. 31, no. 3, pp. 1822–1825, Mar. 2016.

[6] Y. Yang, H. Wang, F. Blaabjerg, and T. Kerekes, "A hybrid power control concept for pv inverters with reduced thermal loading," *IEEE Trans. Power Electron.*, vol. 29, no. 12, pp. 6271–6275, Dec. 2014.

[7] R. Tonkoski, L. A. C. Lopes, and T. H. M. El-Fouly, "Coordinated active power curtailment of grid connected pv inverters for overvoltage prevention," *IEEE Trans. Sustain. Energy*, vol. 2, no. 2, pp. 139–147, Apr. 2011.

[8] N. Femia, G. Petrone, G. Spagnuolo, and M. Vitelli, *Power Electronics and Control Techniques for Maximum Energy Harvesting in Photovoltaic Systems*. CRC Press, 2012.

[9] K. K. Hussein, I. Muta, T. Hoshino, and M. Osakada, "Maximum photovoltaic power tracking: an algorithm for rapidly changing atmospheric conditions," *IEE Proc. -Generation,Transmission Distrib.*, vol. 142, no. 1, pp. 59–64, 1995.

[10] D. Sera, R. Teodorescu, J. Hantschel, and M. Knoll, "Optimized maximum power point tracker for fast-changing environmental conditions," *IEEE Trans. Ind. Electron.*, vol. 55, no. 7, pp. 2629–2637, Jul. 2008.

[11] S. Kjær, "Evaluation of the "hill climbing" and the "incremental conductance" maximum power point trackers for photovoltaic power systems," *IEEE Trans. Energy Convers.*, vol. 27, no. 4, pp. 922–929, Dec. 2012.

[12] N. Femia, D. Granozio, G. Petrone, G. Spagnuolo, and M. Vitelli, "Predictive & adaptive mppt perturb and observe method," *IEEE Trans. Aerosp. Electron. Syst.*, vol. 43, no. 3, pp. 934–950, Jul. 2007.

[13] H. Häberlin, *Photovoltaics: System Design and Practice*. Chichester, UK: John Wiley & Sons, Ltd, feb 2012.

[14] W. Xiao, W. Dunford, P. Palmer, and A. Capel, "Regulation of photovoltaic voltage," *IEEE Trans. Ind. Electron.*, vol. 54, no. 3, pp. 1365–1374, Jun. 2007.

[15] J. Kivimäki, S. Kolesnik, M. Sitbon, T. Suntio, and A. Kuperman, "Revisited perturbation frequency design guideline for direct fixed-step maximum power point tracking algorithms," *IEEE Trans. Ind. Electron.*, pp. 1–1, 2017.

[16] J. Kivimäki, S. Kolesnik, M. Sitbon, T. Suntio, and A. Kuperman, "Design guidelines for multi-loop perturbative maximum power point tracking algorithms," *IEEE Trans. Power Electron.*, pp. 1–1, 2017.

[17] J. Kivimäki, M. Sitbon, S. Kolesnik, A. Kuperman, and T. Suntio, "Sampling frequency design to optimizing MPP-tracking performance for open-loop-operated converters," in *IECON 2016 - 42nd Annu. Conf. IEEE Ind. Electron. Soc.* IEEE, Oct. 2016, pp. 3093–3098.

[18] T. Esram, J. Kimball, P. Krein, P. Chapman, and P. Midya, "Dynamic maximum power point tracking of photovoltaic arrays using ripple correlation control," *IEEE Trans. Power Electron.*, vol. 21, no. 5, pp. 1282–1291, Sep. 2006.

[19] T. Suntio, J. Leppäaho, J. Huusari, and L. Nousiainen, "Issues on solar-generator interfacing with current-fed mpp-tracking converters," *IEEE Trans. Power Electron.*, vol. 25, no. 9, pp. 2409–2419, sep 2010.

[20] J. Viinamäki, A. Kuperman, J. Jokipii, T. Messo, T. Suntio, and M. Sitbon, "Comprehensive dynamic analysis of photovoltaic generator interfacing DC-DC boost power stage," *IET Renew. Power Gener.*, vol. 9, no. 4, pp. 306–314, May 2015.

[21] L. Nousiainen, J. Puukko, A. Mäki, T. Messo, J. Huusari, J. Jokipii, J. Viinamäki, D. T. Lobera, S. Valkealahti, and T. Suntio, "Photovoltaic generator as an input source for power electronic converters," *IEEE Trans. Power Electron.*, vol. 28, no. 6, pp. 3028–3038, Jun. 2013.

[22] M. Sitbon, J. Leppaaho, T. Suntio, and A. Kuperman, "Dynamics of photovoltaic-generator-interfacing voltage-controlled buck power stage," *IEEE J. Photovoltaics*, vol. 5, no. 2, pp. 633–640, Mar. 2015.

[23] M. Eroglu S., Toprak S., Urgan O, MD, Ozge E. Onur, MD, Arzu Denizbasi, MD, Haldun Akoglu, MD, Cigdem Ozpolat, MD, Ebru Akoglu, *Modern Control Engineering*, 2012, vol. 33.

[24] T. Suntio, J. Leppäaho, J. Huusari, and L. Nousiainen, "Issues on solar-generator interfacing with current-fed mpp-tracking converters," *IEEE Trans. Power Electron.*, vol. 25, no. 9, pp. 2409–2419, Sep. 2010.